第 43 卷 第 19 期/2023 年 10 月/光学学报 研究论文

光学学报

X射线球面弯晶成像性能分析及实验测试

钟肖彤[1,2]，刘会亚[3*]，董全力[1,4**]，康宁[3]，张杰[4,5]

[1]哈尔滨工业大学（威海）理学院，山东 威海 264209；

[2]哈尔滨工业大学物理学院，黑龙江 哈尔滨 150001；

[3]中国科学院上海光学精密机械研究所高功率激光物理联合实验室，上海 201800；

[4]上海交通大学 IFSA 协同创新中心，上海 200240；

[5]中国科学院物理研究所北京凝聚态物理国家研究中心，北京 100190

摘要 在惯性约束聚变及实验室天体物理研究中，均需要对等离子体的形态进行清晰的成像，同时具有单色、高分辨、大视场的X射线球面弯晶背光成像是其中一项关键的诊断技术。本文首先对球面弯晶背光成像技术的成像性能进行分析，获得了空间分辨率、成像效率等性能参数随成像系统设计参数变化的关系。在此基础上，利用神光II高功率激光辐照Si靶，激发产生1.865 keV的Heα线，对球面弯晶背光成像系统的性能进行实验验证。实验得到清晰的网格图像和生物样品图像，实验结果与理论计算值相符，成像分辨率达到4.8 μm。该工作满足X射线弯晶成像高分辨率的要求，可用于惯性约束聚变等相关实验中激光等离子体的精密诊断。

关键词 X射线；球面弯晶；背光成像；空间分辨

中图分类号 O434 **文献标志码** A **DOI**：10.3788/AOS230632

1 引 言

惯性约束聚变研究中的物理过程十分复杂，需要发展多种诊断技术对聚变过程中的温度、密度等物理量进行研究[1]。得益于X射线源、X射线光学及探测技术的发展，在近几十年中X射线成像技术不断成熟，针孔成像、X射线显微镜、球面弯晶等X射线成像技术得到了发展。但传统的针孔成像分辨率较低[2]，KB、Wolter显微镜制作工艺复杂、应用困难[3-5]，球面弯晶成像系统不仅结构简单且能够同时实现高空间分辨和窄能谱分辨[6-7]。如今利用球面弯晶对成像物体进行自发光或背光成像已经成为高能量密度物理研究中的重要诊断方式，在Nike KrF、OMEGA、EAST、Hercules等大型激光装置上均得到应用[7-10]。球面弯晶成像技术能够实现一维光谱分辨成像、二维单色自发光成像和二维单色背光成像[11-12]。相比于自发光成像，球面弯晶背光成像对背光源辐射功率的要求更低，且能够实现更高空间分辨和更窄能谱分辨，在流体力学不稳定性测量、烧蚀界面轨迹测量等方面有着广泛的应用[13-17]。

本文从球面弯晶背光成像系统的基本原理出发，分析了单色近正入射球面弯晶背光成像系统的成像性能，着重讨论了影响成像空间分辨率的因素，并在神光II高功率激光装置上进行在线实验验证，获得高分辨率的图像，为进一步研究惯性约束聚变过程中的物理问题奠定了基础。

2 成像基本原理

球面弯晶是成像系统的核心元件，具有单色分光和聚焦成像的双重功能。当复色X射线入射到晶体上时，只有满足Bragg方程的那部分X射线能够被晶体中的原子反射回来从而发生干涉相长，即

$$2d\sin\theta = n\lambda, \tag{1}$$

式中：d为晶格常数；θ为Bragg角；n为衍射级次；λ为X射线波长。由Bragg方程可知，当晶体晶面及Bragg角确定后，能够发生干涉相长的X射线波长也随之确定下来。由布拉格公式可以推导出成像系统的相对光谱带宽[13]，表示为

$$\frac{\Delta\lambda}{\lambda}\approx\frac{\Delta x}{R}\cot\theta, \tag{2}$$

式中：Δx为背光源的大小；R为球面弯晶的曲率半径。通常认为成像系统的相对光谱带宽在10^{-4}～10^{-3}范围内时，可获得成像物体的单色图像。

借助罗兰圆结构描述球面弯晶的成像特性，球面

收稿日期：2023-03-06；**修回日期**：2023-04-12；**录用日期**：2023-05-06；**网络首发日期**：2023-06-28

基金项目：国家自然科学基金（12034020）、山东省自然科学基金重大基础研究项目（ZR2019ZD44）、中国科学院战略性先导科技专项A类（XDA25030300）

通信作者：*liuhy@siom.ac.cn；**qldong@aphy.iphy.ac.cn

晶体的半径与罗兰圆的直径相当，位于罗兰圆上的光源经过球面弯晶衍射和聚焦后仍会聚在罗兰圆上。但将光源放置在罗兰圆内，可获得更大的集光立体角，系统的成像效率更高[18]。球面弯晶成像系统示意图如图1(a)所示，背光源照射在成像物体上，携带成像物体信息的X射线以Bragg角入射到球面弯晶上，经球面弯晶衍射和反射后被探测器接收，从而得到成像物体的二维像。由几何光学成像公式可以分别得到背光源和成像物体的物像关系[13]，表示为

$$\begin{cases}\dfrac{1}{p}+\dfrac{1}{q_{\mathrm{m}}}=\dfrac{2}{R\sin\theta}\\ \dfrac{1}{p}+\dfrac{1}{q_{\mathrm{s}}}=\dfrac{2\sin\theta}{R}\end{cases},\tag{3}$$

$$\begin{cases}\dfrac{1}{a}+\dfrac{1}{b_{\mathrm{m}}}=\dfrac{2}{R\sin\theta}\\ \dfrac{1}{a}+\dfrac{1}{b_{\mathrm{s}}}=\dfrac{2\sin\theta}{R}\end{cases},\tag{4}$$

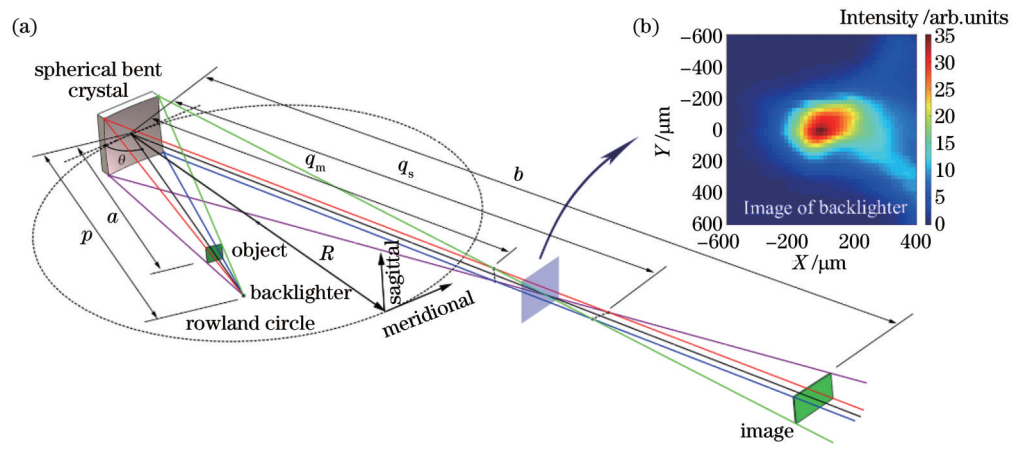

图1　球面弯晶成像系统。(a)系统结构示意图；(b)实验探测到的背光源的像

Fig. 1　Spherically curved crystal imaging system. (a) Schematic diagram of the system; (b) image of the backlight detected in the experiment

式中：p为背光源到晶体的距离；a为成像物体到晶体的距离；q_{m}、q_{s}分别为背光源在子午面和弧矢面上的像距；b_{m}、b_{s}分别为成像物体在子午面和弧矢面上的像距。

3　系统性能分析

3.1　系统参数对成像性能的影响

放大率、视场、空间分辨率、成像效率是衡量球面弯晶背光成像系统性能的重要物理量。把成像物体置于背光源到球面弯晶的光路上，将探测器放在距弯晶b处就可得到物体的二维阴影图像。对成像光路进行分析，可求出探测器上接收到的物像在子午和弧矢平面的放大倍数[19]分别为

$$\begin{cases}M_{\mathrm{m}}=\dfrac{b-q_{\mathrm{m}}}{p-a}\times\dfrac{p}{q_{\mathrm{m}}}\\ M_{\mathrm{s}}=\dfrac{q_{\mathrm{s}}-b}{p-a}\times\dfrac{p}{q_{\mathrm{s}}}\end{cases}。\tag{5}$$

成像系统的视场大小主要由晶体尺寸D_{c}决定，考虑背光源的大小Δx，球面弯晶背光成像的视场[16]为

$$S_{\mathrm{FOV}}=\frac{p-a}{p}D_{\mathrm{c}}+\frac{a}{p}\Delta x。\tag{6}$$

几何像差和衍射极限限制了球面弯晶背光成像系统的空间分辨率。对于X射线波段的电磁波，由衍射极限影响的空间分辨率仅为0.1～1 nm，故可以忽略衍射极限的影响，仅考虑几何像差对空间分辨率的影响[15]。在像差的影响下，物方的一个点在像方会变成一个弥散斑，其弥散斑的长和宽决定了像面上的空间分辨率。基于球面镜成像像差理论和背光成像的原理，得到子午方向和弧矢方向的空间分辨率[20-22]为

$$\begin{cases}\sigma_{\mathrm{m}}=\dfrac{\Delta x\cdot a}{M_{\mathrm{m}}(p-a)}\cdot\dfrac{b-b_{\mathrm{m}}}{b_{\mathrm{m}}}=\\ \qquad\Delta x\dfrac{2ab-bR\sin\theta-aR\sin\theta}{2pb-(p+b)R\sin\theta}\\ \sigma_{\mathrm{s}}=\dfrac{\Delta x\cdot a}{M_{\mathrm{s}}(p-a)}\cdot\dfrac{b-b_{\mathrm{s}}}{b_{\mathrm{s}}}=\\ \qquad\Delta x\dfrac{aR-2ab\sin\theta+bR}{2pb\sin\theta-(p+b)R}\end{cases}。\tag{7}$$

图2给出了子午面和弧矢面的放大率和空间分辨率随探测器位置b的变化关系，良好的成像质量要求同时兼顾大放大倍数和高空间分辨。从图2可以看出，随着b的增大，放大倍数不断增大，空间分辨率逐渐提高。当探测器距弯晶3700 mm时，成像系统的放大率约为16，系统的分辨率约为4.4 μm。

成像系统的效率k[11]定义为图像亮度I和光源亮度I_0的比值，即

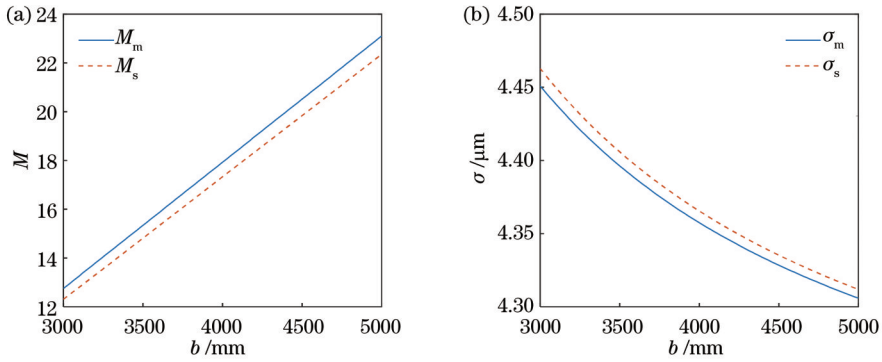

图 2　系统性能参数的理论值。(a) 放大率;(b) 分辨率

Fig. 2　Theoretical values of the system performance parameters. (a) Magnification; (b) resolution

$$k=\frac{I}{I_0}=\frac{\eta\Omega}{M_m M_s},\tag{8}$$

式中:η 为系统的反射效率;Ω 为集光立体角;M_m、M_s 分别为系统子午面和弧矢面的放大率。在球面弯晶背光成像系统中,反射效率 η[13,15]受限于球面晶体的反射率以及成像系统对光谱带宽,表示为

$$\eta=\eta_{erf}\cdot\eta_{line}=\frac{R_{int}}{\left(\Delta\lambda_{line}/\lambda\right)\tan\theta}\cdot\frac{\Delta\lambda/\lambda}{\Delta\lambda_{line}/\lambda},\tag{9}$$

式中:R_{int} 为晶体的积分反射率,$R_{int}=R_p\Delta\theta_B$,$R_p$ 为晶体反射率的峰值,$\Delta\theta_B$ 为晶体摇摆曲线的半峰全宽;$\Delta\lambda_{line}/\lambda$ 为用于背光的 X 射线的相对谱线宽度;$\Delta\lambda/\lambda$ 为系统的相对光谱带宽。由布拉格公式可以求得 $\Delta\lambda/\lambda=\Delta x/R\tan\theta$,代入式(9)可以得到成像系统的反射效率 η,表示为

$$\eta=\frac{R_{int}}{\left(\Delta\lambda_{line}/\lambda\right)^2\tan^2\theta}\cdot\frac{\Delta x}{R}。\tag{10}$$

集光立体角 Ω[22]的计算式为

$$\Omega=\frac{\pi(\Delta x)^2}{4(p-a)^2}。\tag{11}$$

代入可得成像系统的效率为

$$k=\frac{\pi R_{int}(\Delta x)^3}{4M_m M_s\left(\Delta\lambda_{line}/\lambda\right)^2\tan^2\theta R(p-a)^2}。\tag{12}$$

成像系统的空间分辨率和效率是相互制约的关系,且均受到背光源尺寸的影响,图 3 给出了它们随背光源尺寸的变化关系。随着背光源尺寸的增大,空间分辨率呈线性降低,同时系统的成像效率呈幂次方增长。在实际的成像实验中,在确保图像亮度适宜的前提下,尽可能使用小尺寸的背光源可显著提升成像系统的分辨率。

当 X 射线照射在弯晶的边缘处时,入射角的大小略有变化,从而引起边缘处空间分辨率的变化。由空间几何关系不难推出此时的入射角为

$$\theta'\approx\arcsin\frac{p\sin\theta}{\sqrt{\frac{M^2}{4}+p^2-Mp\cos\theta}}。\tag{13}$$

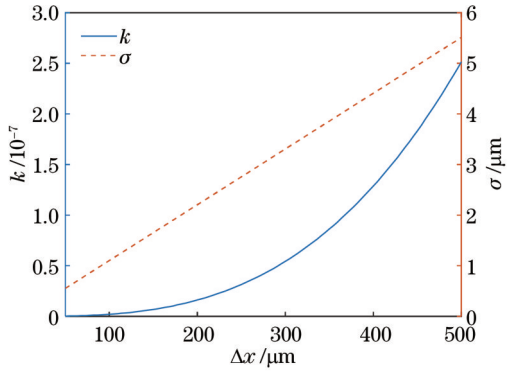

图 3　空间分辨率和成像效率随光源尺寸的变化曲线

Fig. 3　Curves of spatial resolution and imaging efficiency as a function of backlight size

图 4 给出了弯晶中心和边缘处成像时的空间分辨率曲线。随着入射角的增大,空间分辨率变高,但弯晶边缘处的分辨率始终低于中心处的分辨率。因此,在确保视场大小适中的条件下,尽可能使弯晶中心部分成像于探测器的中心,可实现高分辨率成像。

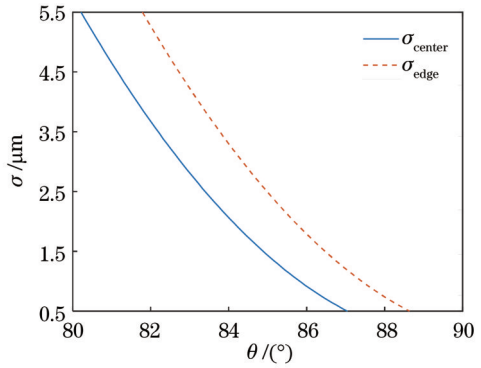

图 4　弯晶中心和边缘处的空间分辨率曲线

Fig. 4　Curves of spatial resolution at the center and edge of the spherically curved crystal

3.2　像差对成像性能的影响

实际的光学系统中存在着各种像差,像差影响着成像系统的成像质量。通过适当地设计成像系统的参数可以将像差校正在一定的限度范围内,得到近似完

善的像。球面弯晶背光成像系统可以得到单色的X射线，因此不存在色差。球差是影响弯晶分辨率的主要因素，通过计算一阶球差得到了分辨率[式(7)]。下面对该成像系统的彗差、像散及畸变进行简要分析。

光轴外的物点发出的光经光学系统折射后，在像面上成形状如彗星的光斑，这种像差就是彗差。阿贝正弦条件给出了消除彗差的条件，对于球面弯晶背光成像系统，位于罗兰圆上的光源发出的光经球面弯晶反射后会聚于罗兰圆上的对称点处，此时球面弯晶背光系统满足阿贝正弦条件，消除了彗差。

像散是轴外光束在子午面和弧矢面上无法会聚于同一点而引起的像差。由球面弯晶背光成像系统的物像关系[式(3)]可以得出，该成像系统在子午面和弧矢面上分别聚焦，故存在像散。在本文设置的系统参数下，子午面和弧矢面的焦距分别为3352 mm和4096 mm，故将探测器放在两个焦点之间以校正像散。另外可以通过减小视场、使用超环面弯镜或配对球面弯晶来校正像散[23]。

子午面和弧矢面的放大率不一致将会引起图像的畸变。在本文的系统参数设置下，子午面和弧矢面的放大率分别为16.41和15.85，故该系统成像存在着轻微的畸变。在球面弯晶背光成像系统中，将子午面放大率与弧矢面放大率相等的位置称为最佳成像位置，通过将探测器放在最佳成像位置处可以获得无畸变的图像。

3.3　球面弯晶面形误差对成像性能的影响

球面弯晶自身的缺陷会影响成像系统的成像性能，下面简要分析球面弯晶半径R的微小误差ΔR对系统放大率及分辨率的影响。

子午面和弧矢面的放大率与焦距q_m、q_s有关，焦距q_m、q_s的计算式中又包含弯晶的曲率半径R，将式(3)代入式(5)，得到放大率与弯晶曲率半径的关系式

$$\begin{cases} M_m = \dfrac{2pb-(p+b)R\sin\theta}{(p-a)R\sin\theta} \\ M_s = \dfrac{2pb\sin\theta-(p+b)R}{(p-a)R} \end{cases}。\tag{14}$$

由放大率公式可以推导出球面弯晶曲率半径的微小误差引起的放大率相对变化率为

$$\begin{cases} \dfrac{\Delta M_m}{M_m} = \dfrac{2(p+b)R\sin\theta-2pb}{2pb-(p+b)R\sin\theta}\cdot\dfrac{\Delta R}{R} \\ \dfrac{\Delta M_s}{M_s} = \dfrac{2(p+b)R-2pb\sin\theta}{2pb\sin\theta-(p+b)R}\cdot\dfrac{\Delta R}{R} \end{cases}。\tag{15}$$

保持系统参数不变，假设弯晶曲率半径的微小误差ΔR在[−5 mm，5 mm]之间，得到放大率的相对变化率曲线如图5(a)所示，相对变化率最大为1.13%，因此，在实验中可以忽略弯晶曲率半径的微小误差对放大率带来的影响。

用同样的方法可以得到空间分辨率的相对变化率

$$\begin{cases} \dfrac{\Delta\sigma_m}{\sigma_m} = \dfrac{2\Delta Rb^2(a-p)\sin\theta}{\left[2pb-(p+b)R\sin\theta\right]\left[2ab-(a+b)R\sin\theta\right]} \\ \dfrac{\Delta\sigma_s}{\sigma_s} = \dfrac{2\Delta Rb^2(p-a)\sin\theta}{\left[2pb\sin\theta-(p+b)R\right]\left[(a+b)R-2ab\sin\theta\right]} \end{cases}。\tag{16}$$

空间分辨率的相对变化率曲线如图5(b)所示，相对空间分辨率最大为0.86%，因此，在实验中可以忽略弯晶曲率半径的微小误差对空间分辨率带来的影响。

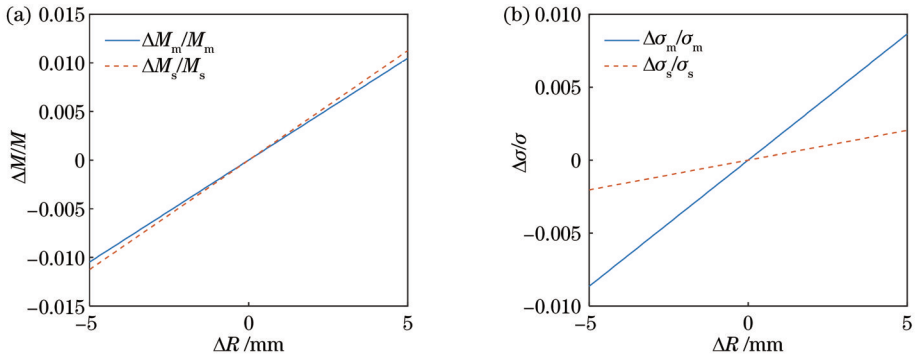

图5　弯晶半径误差对成像性能的影响。(a)放大率；(b)分辨率

Fig. 5　Influence of the spherically curved crystal radius error on imaging performance. (a) Magnification; (b) resolution

4　实验验证

4.1　实验参数和设置

为了验证弯晶成像系统的成像性能，在中国科学院上海光学精密机械研究所的神光II高功率激光装置上展开了在线实验验证。激光能量为10～200 J，激光脉宽为100 ps，波长为351 nm。利用8路激光中的一路辐照Si平面靶，选用的Si靶发出的1.865 keV的Heα线作为背光源，其波长为0.665 nm。采用石英晶体(α-quartz $10\bar{1}0$)压制成曲率半径为433 mm的球面弯晶，$2d$=0.6687 nm，则Bragg角为83.8°。X射线源距离弯晶的距离为360 mm，成像物体距离弯晶的距离为230 mm，探测器放置在了距弯晶3700 mm左右的位置，由实验测得背光源的大小约为200 μm。探测器

分别使用了 Image Plate 和 Andor 的 X 射线 CCD，两者的自身分辨率分别为 50 μm 和 13.5 μm。在对背光源成像和调试阶段使用 Image Plate 作为探测器，正式成像阶段使用 Andor 的 X 射线 CCD。实验中，在成像物体的位置放置了 1500 目的 Cu 网格，其周期为 17 μm。

4.2　实验结果及分析

成像结果如图 6(a)所示，从 CCD 成像结果上可以看到清晰的网格，分辨率明显优于 200 μm 的背光源大小。成像边缘位置存在着轻微的变形，这可能是晶体在压弯过程中产生的边界应力造成了晶面间距发生改变，或晶体在固定过程中因受力不均匀带来的面形误差引起的。为了得到成像系统的分辨率，选取成像结果中的部分网格进行边缘扩散函数(ESF)拟合，拟合结果如图 6(b)所示，拟合函数为

$$I_{\mathrm{ESF}}=I_0\cdot\mathrm{erf}\left(\frac{x}{\sigma}\right)+a_0+a_1x。\tag{17}$$

其中，

$$\mathrm{erf}\left(\frac{x}{\sigma}\right)=\frac{2}{\pi}\int_0^{x/\sigma}\exp\left(-t^2\right)\mathrm{d}t。\tag{18}$$

拟合可以得到 2σ=4.8 μm，即分辨率为 4.8 μm。

为了得到更为精确的结果，定义图 7(a)中的圆圈区域内为最佳成像区域，其中五角星标记位置处为该区域的中心。图 7(b)给出了分辨率随偏离最佳成像区域的距离的变化关系。随着偏离最佳成像区域的距离的增加，分辨率整体呈下降趋势，且弧矢面的分辨率略低于子午面的分辨率。在距最佳成像位置 200 μm 的范围内，子午方向的平均分辨率为 4.7 μm，弧矢方向的平均分辨率为 4.83 μm。

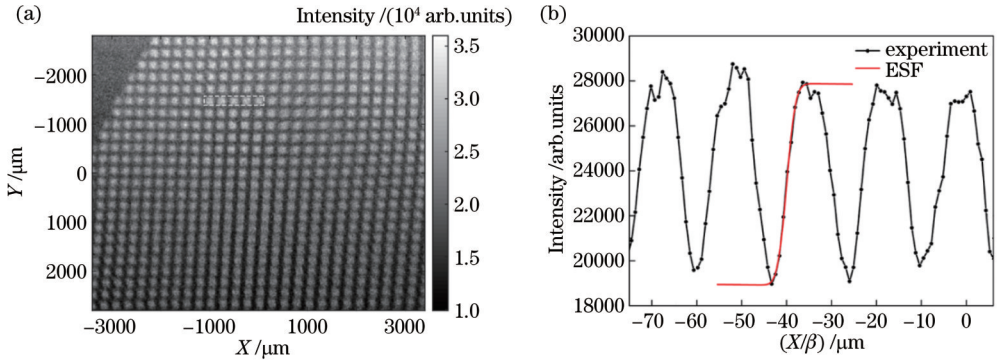

图 6　网格成像结果及分析。(a)1500 目 Cu 网格成像结果；(b)ESF 拟合结果

Fig. 6　Grid imaging results and analysis. (a) 1500 mesh Cu grid imaging result; (b) ESF fitting results

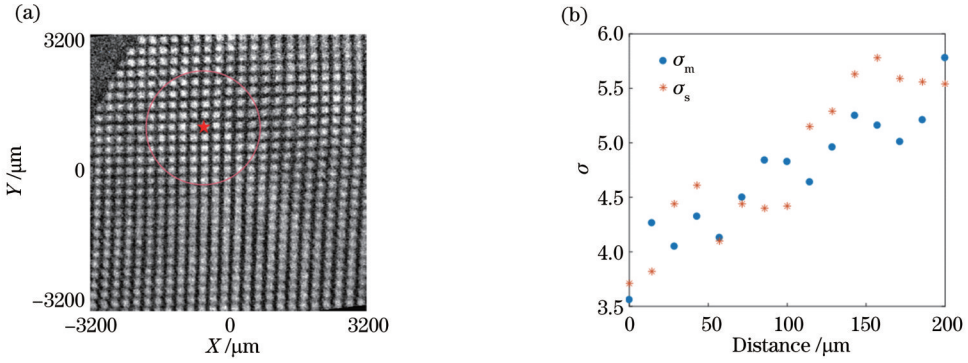

图 7　网格成像结果及分析。(a)1500 目 Cu 网格成像结果；(b)分辨率随偏离最佳成像区域距离的变化关系

Fig. 7　Grid imaging results and analysis. (a) 1500 mesh Cu grid imaging results; (b) relationship between resolution and distance away from the best imaging area

用同样的方法还拟合了位于成像结果边缘位置的网格，得到子午方向的分辨率为 6.12 μm，弧矢方向的分辨率为 9.95 μm。边缘位置的分辨率相比最佳成像区域内有较大幅度的降低，这是由于成像系统在边缘位置存在一定程度的像散和畸变以及网格自身形变而引起的分辨率的降低。此外，由于激光等离子体的不稳定性会产生几十 keV 到几百 keV 的超热电子，这些超热电子及其产生的韧致辐射部分会到达探测器，给成像带来噪声。另外，其他波段的 X 射线在光管道中散射，也会被探测器接收，同样产生成像噪声。在后续的实验中可通过设计合适的滤片组，并增加准直模块来减少这些射线引起的噪声，提高信噪比。

利用此套实验装置，在线对昆虫的翅翼进行了成像。昆虫采用了斑衣蜡蝉的翅翼标本，安装在靶架上，如图 8 所示。成像结果如图 9(a)所示，从成像结果上

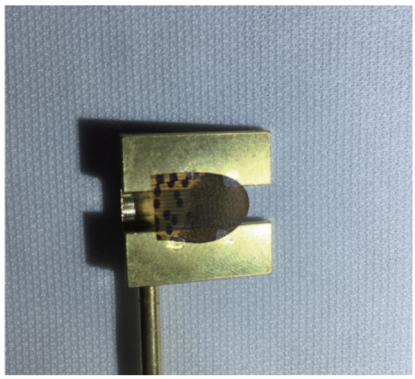

图 8　斑衣蜡蝉标本

Fig. 8　Sample of *lycorma delicatula*

可以到斑衣蜡蝉翅膀上的主脉、径脉和横脉，近似呈现四方形。但图像的信噪比较低，影响了对蝉翼成像细节的观察，故采用 Retinex 算法对图像进行处理，得到增强图像如图 9(b)所示。Retinex 算法对图像的处理过程如图 10 所示，通过对数运算将输入图像的入射分量和反射分量分离，计算图像像素点的加权平均实现对照射图像估计，将入射分量除去，只保留反射分量，再对图像进行高斯滤波得到增强后的图像，最后进行对比度增强并输出图像。斑衣蜡蝉翅翼的径脉和横脉的宽度在 35～45 μm 之间，径脉的直径略大于横脉的直径，从图 9(b)可以看到清晰的脉络，说明该系统可实现对生物样本的高分辨率成像。

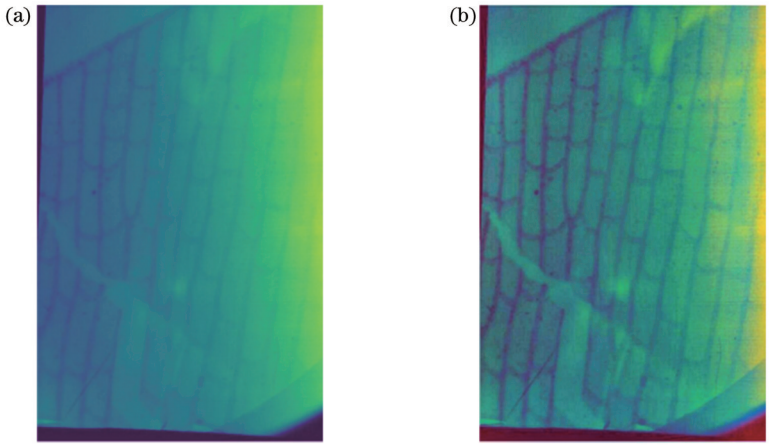

图 9　生物标本成像结果。(a)单能 X 射线成像结果；(b)Retinex 算法处理结果

Fig. 9　Images of biological sample. (a) Monochromatic X-ray imaging results of the wings; (b) processing results of the Retinex algorithm

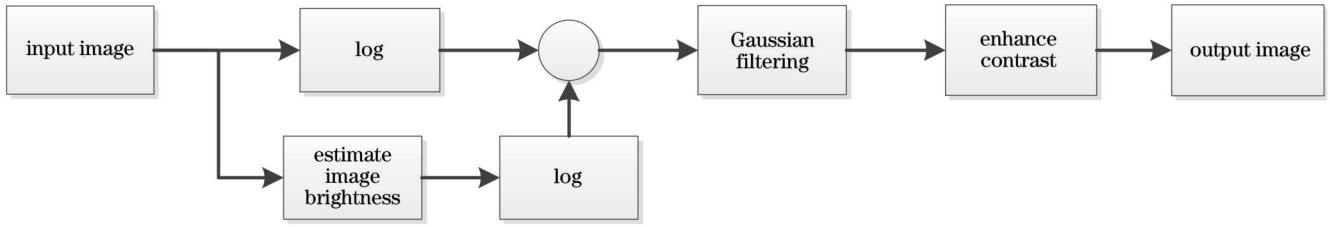

图 10　Retinex 算法流程图

Fig. 10　Flow chart of Retinex algorithm

5　结　　论

本文对球面弯晶背光成像系统的性能进行分析，给出了放大率、空间分辨率及成像效率随系统参数的变化曲线，分析了像差和弯晶面形误差对系统成像性能的影响。在神光 II 高功率激光装置上展开实验，分别对 1500 目的 Cu 网格和斑衣蜡蝉的翅翼标本进行成像，均得到清晰的图像，该球面弯晶背光成像系统的分辨率最高可达 4.8 μm，满足了高分辨率成像的要求。在后续的实验中可通过进一步减小背光源的尺寸，在探测器前放置滤片等方式进一步提升成像系统的空间分辨能力。

参　考　文　献

[1] 王立锋，叶文华，陈竹，等. 激光聚变内爆流体不稳定性基础问题研究进展[J]. 强激光与粒子束，2021，33(1)：012001.
Wang L F, Ye W H, Chen Z, et al. Review of hydrodynamic instabilities in inertial confinement fusion implosions[J]. High Power Laser and Particle Beams, 2021, 33(1): 012001.

[2] 白晓红，白永林，刘百玉，等. 神光原型诊断设备：门控针孔分幅相机的研制[J]. 光学 精密工程，2011，19(2)：367-373.
Bai X H, Bai Y L, Liu B Y, et al. SG diagnostic equipment: gating pinhole framing camera[J]. Optics and Precision Engineering, 2011, 19(2): 367-373.

[3] Werner W. Imaging properties of Wolter I type X-ray telescopes

[J]. Applied Optics, 1977, 16(3): 764-773.
[4] Pickworth L A, McCarville T, Decker T, et al. A Kirkpatrick-Baez microscope for the national ignition facility[J]. Review of Scientific Instruments, 2014, 85(11): 11D611.
[5] 伊圣振, 司昊轩, 黄秋实, 等. 激光惯性约束聚变X射线诊断用多通道Kirkpatrick-Baez成像系统研究进展[J]. 光学学报, 2022, 42(11): 1134007.
Yi S Z, Si H X, Huang Q S, et al. Research progress of multi-channel Kirkpatrick-Baez microscope for X-ray diagnostics in laser inertial confinement fusion[J]. Acta Optica Sinica, 2022, 42(11): 1134007.
[6] 施军, 赵雨鑫, 黎淼, 等. 球面弯曲晶体硬X射线透射成像[J]. 光学学报, 2022, 42(11): 1134011.
Shi J, Zhao Y X, Li M, et al. Hard X-ray transmission imaging of spherical curved crystal[J]. Acta Optica Sinica, 2022, 42(11): 1134011.
[7] Aglitskiy Y, Lehecka T, Obenschain S, et al. High-resolution monochromatic X-ray imaging system based on spherically bent crystals[J]. Applied Optics, 1998, 37(22): 5253-5261.
[8] Stoeckl C, Fiksel G, Guy D, et al. A spherical crystal imager for OMEGA EP[J]. Review of Scientific Instruments, 2012, 83(3): 033107.
[9] Shi Y J, Wang F D, Wan B N, et al. Imaging X-ray crystal spectrometer on EAST[J]. Plasma Physics and Controlled Fusion, 2010, 52(8): 085014.
[10] Pikuz T A, Faenov A Y, Skobelev I Y, et al. Highly efficient X-ray imaging and backlighting schemes based on spherically bent crystals[J]. Proceedings of SPIE, 2004, 5196: 362-374.
[11] Koch J A, Aglitskiy Y, Brown C, et al. 4.5- and 8-keV emission and absorption X-ray imaging using spherically bent quartz 203 and 211 crystals (invited)[J]. Review of Scientific Instruments, 2003, 74(3): 2130-2135.
[12] Belyaev L M, Gil′varg A B, Mikhaĭlov Y A, et al. X-ray photography of laser plasmas with the aid of analyzer crystals bent to form second-order surfaces[J]. Soviet Journal of Quantum Electronics, 1976, 6(9): 1121-1122.
[13] Sinars D B, Bennett G R, Wenger D F, et al. Evaluation of bent-crystal X-ray backlighting and microscopy techniques for the Sandia Z machine[J]. Applied Optics, 2003, 42(19): 4059-4071.
[14] Brown C, Seely J, Feldman U, et al. X-ray imaging of targets irradiated by the Nike KrF laser[J]. Review of Scientific Instruments, 1997, 68(1): 1099-1102.
[15] Schollmeier M S, Geissel M, Shores J E, et al. Performance of bent-crystal X-ray microscopes for high energy density physics research[J]. Applied Optics, 2015, 54(16): 5147-5161.
[16] 陈伯伦, 杨正华, 李晋, 等. 用于烧蚀过程界面轨迹测量的球面弯晶成像系统[J]. 光学学报, 2022, 42(11): 1134012.
Chen B L, Yang Z H, Li J, et al. Spherical bending crystal imaging system for measuring interface trajectory in ablation process[J]. Acta Optica Sinica, 2022, 42(11): 1134012.
[17] Turner D C, Knight L V, Mena A R, et al. Focusing crystal von Hamos spectrometers for XRF applications[J]. Advances in X-ray Analysis, 2001, 44: 329-335.
[18] Brown C, Seely J, Feldman U, et al. High-resolution X-ray imaging of planar foils irradiated by the Nike KrF laser[J]. Physics of Plasmas, 1997, 4(5): 1397-1401.
[19] Flora F, Bollanti S, Lai A, et al. Novel portable high-luminosity monochromatically tunable X-ray microscope[J]. Proceedings of SPIE, 2001, 4504: 240-252.
[20] Young B K F, Osterheld A L, Price D F, et al. High-resolution X-ray spectrometer based on spherically bent crystals for investigations of femtosecond laser plasmas[J]. Review of Scientific Instruments, 1998, 69(12): 4049-4053.
[21] Bennett G R, Sinars D B, Wenger D F, et al. High-brightness, high-spatial-resolution, 6.151 keV X-ray imaging of inertial confinement fusion capsule implosion and complex hydrodynamics experiments on Sandia's Z accelerator (invited)[J]. Review of Scientific Instruments, 2006, 77(10): 10E322.
[22] 阳庆国, 李泽仁, 彭其先, 等. 激光驱动X射线单色背光照相系统优化设计[J]. 强激光与粒子束, 2008, 20(12): 1983-1988.
Yang Q G, Li Z R, Peng Q X, et al. Optimum design of laser-driven-monochromatic X-ray backlighting system[J]. High Power Laser and Particle Beams, 2008, 20(12): 1983-1988.
[23] Bitter M, Hill K W, Scott S, et al. Wide-angle point-to-point X-ray imaging with almost arbitrarily large angles of incidence[J]. The Review of Scientific Instruments, 2008, 79(10): 10E927.

Performance Analysis and Experimental Test of X-Ray Spherically Curved Crystal Imaging

Zhong Xiaotong[1,2], Liu Huiya[3*], Dong Quanli[1,4**], Kang Ning[3], Zhang Jie[4,5]

[1]*Department of Science, Harbin Institute of Technology (Weihai), Weihai* 264209, *Shandong, China*;
[2]*Department of Physics, Harbin Institute of Technology, Harbin* 150001, *Heilongjiang, China*;
[3]*National Laboratory on High Power Lasers and Physics, Shanghai Institute of Optics and Fine Mechanics, Chinese Academy of Sciences, Shanghai* 201800, *China*;
[4]*Collaborative Innovation Center of IFSA, Shanghai Jiao Tong University, Shanghai* 200240, *China*;
[5]*Beijing National Laboratory of Condensed Matter Physics, Institute of Physics, Chinese Academy of Sciences, Beijing* 100190, *China*

Abstract

Objective Due to the insufficient understanding of the complex physical processes during fusion, research on inertial confinement fusion (ICF) has reached a plateau after decades of rapid development. Therefore, the development of diagnostic techniques under extreme transient conditions is crucial to advance the research on ICF. Large amounts of plasma X-rays are generated in the fusion process. Both the continuum and the line spectra of the X-rays contain a large

amount of information about the plasma parameters and the fusion process, including the plasma temperature, density, spatial scale, etc. The diagnosis of high-temperature plasma X-rays is extremely important in the diagnosis of ICF. X-ray spherically curved crystal imaging with monochromatic, high resolution, and large field of view is one of the key diagnostic techniques. Spherically curved crystal imaging technology can achieve one-dimensional spectral resolution imaging, two-dimensional monochromatic self-illumination imaging, and two-dimensional monochromatic backlight imaging. Compared with self-illumination imaging, spherically curved crystal backlight imaging has lower requirements for backlight radiation power and can achieve higher spatial resolution and narrower spectral resolution. The resolution ability of the spherically curved crystal backlight imaging system is an important indicator of this diagnostic method. However, at present, there are still few studies on the spherically curved crystal backlight imaging system in China, and compared with the international best resolution ability, it also needs to be further improved. Therefore, in this paper, the imaging performance of the spherically curved crystal backlight imaging system was analyzed in detail, and the experimental test was carried out on SG-Ⅱ high-power laser device. It is hoped that the resolution of the system can be further improved by the reasonable design of experimental parameters so that the spherically curved crystal backlight imaging system can be used for the precision diagnosis of laser plasma in ICF.

Methods To explore the imaging performance of the spherically curved crystal backlight imaging system, we focused on both theoretical and experimental aspects. In theory, the influences of system parameters, aberration, small error of the bending crystal radius, and other factors on imaging performance were analyzed. The variation curves of performance parameters with each influencing factor were plotted, which provided theoretical support for the analysis of subsequent experimental results. Based on the theoretical analysis, the specific system parameters were determined. The X-ray source was 360 mm away from the curved crystal, and the imaging object was 230 mm away from the curved crystal; the detector was placed about 3700 mm away from the curved crystal, and the size of the backlight was about 200 μm. Then the imaging performance of the imaging system was tested by the SG-Ⅱ high-power laser device. The Heα line of 1.865 keV excited by laser irradiation of the Si target was selected as the backlight source, with a wavelength of 0.665 nm. The quartz crystal, pressed into a spherically curved crystal with a radius of curvature of 433 mm, was the core imaging element. The Image Plate was chosen as the detector for the backlight imaging and system commissioning phase. The Andor X-ray CCD, with its own higher resolution, was chosen as the detector for the formal imaging phase. In order to check the imaging performance of the imaging system, a Cu grid with 1500 meshes was first imaged, and a grid image with a resolution of approximately 4.8 μm was obtained. In order to further validate the imaging performance of the imaging system, cicada wing specimens were imaged, and clear images of cicada wing specimens were obtained using numerical methods.

Results and Discussions Firstly, there were inevitable aberrations in the imaging system which could affect the image quality of the imaging system. Spherical aberration, coma, dispersion, and aberrations in spherically curved crystal backlight imaging systems were theoretically analyzed, and appropriate aberration correction methods were given. The effect of the spherical bend radius error on imaging performance was then investigated, and the equations for the relative rate of change of magnification and spatial resolution caused by the bend radius error were derived. The relative rate of change curves was plotted (Fig. 5). Secondly, experimentally clear grid images were obtained by using a spherically curved crystal imaging system, and the resolution of the grid images was obtained by edge function fitting down to 4.8 μm (Fig. 6). In order to obtain more accurate statistical results, the best imaging position in the grid image was calibrated, and the variation of resolution in the meridional and sagittal directions with deviation from the best imaging position was analyzed (Fig. 7). Within a range of 200 μm from the optimum imaging position, resolutions of down to 4.7 μm in the meridional direction and 4.83 μm in the sagittal direction could be achieved. Even at the edges, where there was a lot of distortion and noise, it was possible to achieve a resolution of 9.95 μm. Finally, in order to validate the imaging performance of the imaging system on biological samples, cicada wing specimens were imaged. However, due to small deviations in the collimation process, the signal-to-noise ratio of the images was relatively low. Data processing of the images using the Retinex algorithm improved the contrast of the images, resulting in clear images of biological specimens (Fig. 9), which proved that the imaging system could also be used for the diagnosis of biological specimens.

Conclusions We presented a theoretical analysis of the imaging performance of the spherically curved crystal backlight imaging system and discussed the effects of system parameters, aberrations, small errors of the bending crystal radius, and other factors on the imaging performance. A theoretical basis was provided for the subsequent design of experimental parameters and analysis of experimental results. In the experiments, the X-ray spherically curved crystal backlight imaging system was constructed by using a quartz crystal. X-ray CCD was chosen as the detector. The experiments were performed by using SG-Ⅱ high-power laser device. Clear images were obtained for

the metal grid and biological samples respectively. Further analysis of the grid images showed that the high spatial resolution of about 4.8 μm could be maintained. Therefore, the spherically curved crystal backlight imaging system is capable of high-resolution imaging over a large field of view and can be used for the precision diagnosis of high-temperature plasma in ICF. In further experiments, we will reduce the effect of noises on an image by adding filters and collimation modules or reducing the size of the backlight to improve the resolution of the spherically curved crystal backlight imaging system.

Key words X-ray; spherically curved crystal; backlight imaging; spatial resolution